PHOTONICS Research

Quenching of second-harmonic generation by epsilon-near-zero media

Chenglin Wang,[1] Ran Shi,[1] Lei Gao,[1,2,5] Alexander S. Shalin,[1,3,4] and Jie Luo[2,6]

[1]School of Optical and Electronic Information, Suzhou City University, Suzhou 215104, China
[2]School of Physical Science and Technology, Soochow University, Suzhou 215006, China
[3]Center for Photonics and 2D Materials, Moscow Institute of Physics and Technology, Dolgoprudny 141700, Russia
[4]Kotel'nikov Institute of Radio Engineering and Electronics of Russian Academy of Sciences (Ulyanovsk branch), Ulyanovsk 432011, Russia
[5]e-mail: leigao@suda.edu.cn
[6]e-mail: luojie@suda.edu.cn

Received 3 April 2023; revised 10 June 2023; accepted 15 June 2023; posted 21 June 2023 (Doc. ID 491949); published 1 August 2023

Epsilon-near-zero (ENZ) media were demonstrated to exhibit unprecedented strong nonlinear optical properties including giant second-harmonic generation (SHG) due to their field-enhancement effect. Here, on the contrary, we report the quenching of SHG by the ENZ media. We find that when a tiny nonlinear particle is placed very close to a subwavelength ENZ particle, the SHG from the nonlinear particle can be greatly suppressed. The SHG quenching effect originates from the extraordinary prohibition of electric fields occurring near the ENZ particle due to evanescent scattering waves, which is found to be universal in both isotropic and anisotropic ENZ particles, irrespective of their shapes. Based on this principle, we propose a kind of dynamically controllable optical metasurface exhibiting switchable SHG quenching effect. Our work enriches the understanding of optical nonlinearity with ENZ media and could find applications in optical switches and modulators.

https://doi.org/10.1364/PRJ.491949

1. INTRODUCTION

Nonlinear optical harmonic generation is of great significance in a broad range of technologies and has been attracting much attention in photonics, chemistry, and biosensing. The understanding and manipulation of nonlinear optical properties of nanostructures is a major issue for realizing nonlinear nanophotonic devices. In the past decades, a lot of efforts have been made to enhance the nonlinear frequency conversion efficiency, including the new materials and systems [1–7]. Recently, with the advent of plasmonics, metamaterials, and metasurfaces that go beyond natural materials in many aspects, significant attention has been devoted to the understanding and the observation of nonlinear optical processes in nanophotonics [1–7]. For boosting the second-harmonic generation (SHG) [8–13], as one of the most important nonlinear optical effects, many approaches have been proposed. For example, through exciting resonance modes like surface plasmon polariton resonances [8], Fano resonances [9], anapole modes [10,11], and bound states in the continuum [12], the fundamental fields inside the nonlinear materials can be greatly enhanced, so as to boost the SHG. Notably, epsilon-near-zero (ENZ) media [7,14–17] with a vanishing permittivity are found to exhibit pronounced nonlinear optical properties [7,18–38]. The ENZ media can provide large field enhancement due to the continuity of the normal component of the electric displacement field across the interface [18,19], and at the same time provide unique opportunities for realizing phase-matching conditions [23,38]. Consequently, the ENZ media can give rise to unprecedented strong nonlinear optical responses including the significantly enhanced SHG [18–22,27–29].

In this work, on the contrary, we demonstrate that the ENZ media can be exploited to "turn off" the SHG of a nonlinear particle. We show that when a tiny nonlinear particle is placed very close to a subwavelength ENZ particle, the SHG conversion efficiency can be reduced by more than 2 orders of magnitude as compared to that from the nonlinear particle alone (Fig. 1). The SHG quenching effect attributes to the extraordinary local evanescent fields occurring near the ENZ particle due to evanescent scattering waves. Remarkably, the prohibition of electric fields appears besides the ENZ particle, and therefore, the SHG from the tiny nonlinear particle placed there would be suppressed. We find that this extraordinary local evanescent field exists for both isotropic and anisotropic ENZ particles, irrespective of their shapes. Furthermore, based on the principle of SHG quenching effect, we propose a kind of dynamically controllable optical metasurface integrated with anisotropic ENZ media, which consist of alternative layers of semiconductor material cadmium oxide (CdO) and phase-change material germanium telluride (GeTe). We find that through changing the phase states of GeTe, the SHG from the metasurface can be switched on or off. Our work demonstrates a feasible approach for controlling nonlinear responses

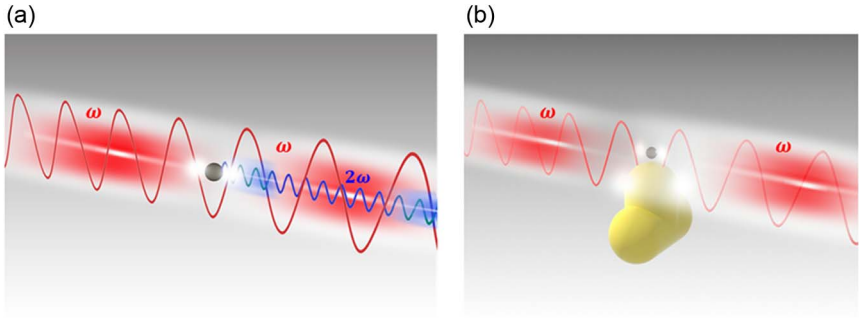

Fig. 1. (a) Schematic illustration of SHG from a tiny nonlinear particle. (b) The SHG is quenched when a linear ENZ particle is placed very close to the tiny nonlinear particle.

with ENZ media, which may find applications in optical switches and modulators.

2. SHG QUENCHING AND THE UNDERLYING PHYSICS

First, to explore the physical mechanism of the unique SHG quenching effect, we begin with a simple configuration comprising a linear ENZ spherical particle (relative permittivity $\varepsilon_e \approx 0$, relative permeability $\mu_e = 1$) and a tiny nonlinear spherical particle (relative permittivity $\varepsilon_n = 2$, relative permeability $\mu_n = 1$) in free space, as illustrated in Fig. 2(a). Both particles are in the deep-subwavelength scale with radii of $r_e = \lambda_0/100$ (ENZ particle) and $r_n = 0.1r_e$ (nonlinear particle), where λ_0 is free-space wavelength. The gap (i.e., edge-to-edge distance) between the two particles is d. The two particles are illuminated by a plane wave propagating along the z direction with electric field $\mathbf{E}_0^{\omega}$ polarized in the x direction.

The SHG of the tiny nonlinear spherical particle can be accounted for by effective surface contribution and characterized by a surface nonlinear current source $\mathbf{J}^{2\omega} = -i2\omega\varepsilon_0 \overleftrightarrow{\chi}_a^{(2)} : \mathbf{E}^{\omega}\mathbf{E}^{\omega}$, where $\overleftrightarrow{\chi}_a^{(2)}$ is the nonlinear susceptibility tensor, and $\mathbf{E}^{\omega}$ is the fundamental frequency electric field inside the nonlinear particle. ε_0 is the permittivity of free space. For isotropic and centrosymmetric materials, the second-order surface susceptibility tensor $\overleftrightarrow{\chi}_a^{(2)}$ can be reduced to only three independent nonzero components $\overleftrightarrow{\chi}_{\perp\perp\perp}^{(2)}$, $\overleftrightarrow{\chi}_{\perp\parallel\parallel}^{(2)}$, and $\overleftrightarrow{\chi}_{\parallel\parallel\perp}^{(2)}$ [39,40]. Here the symbols $\perp$ and $\parallel$ represent the directions perpendicular and parallel to the particle's surface, respectively.

Figure 2(b) shows the scattering cross section of SHG ($SCS^{2\omega}$) from the tiny nonlinear particle when it is successively moved from position 1 to position 5 along the trajectory $1 \rightarrow 2 \rightarrow 3 \rightarrow 4 \rightarrow 5$ [green curves in Fig. 2(a)]. Along the trajectory $1 \rightarrow 4$, the edge-to-edge distance d is kept unchanged at $r_e/20$, and position 5 is at a distance of $6r_e$ from the ENZ sphere's center. Here we assume that the nonlinear susceptibility of the tiny particle is several orders of magnitude larger than that of the ENZ particle, and therefore, the nonlinear response of the ENZ particle is negligible. Such an assumption is reasonable when using appropriate optical materials [30], as we will show in the following practical implementations. The calculation is performed using the finite-element software COMSOL Multiphysics. The solid blue lines and red dots denote the normalized $SCS^{2\omega}$ of the cases with and without the ENZ particle, respectively. The latter case is normalized to 1. As expected, in the absence of the ENZ particle, the $SCS^{2\omega}$ will not change as varying the position under the illumination of a plane wave. Interestingly, we observe that the presence of the ENZ particle has a great influence on the SHG conversion

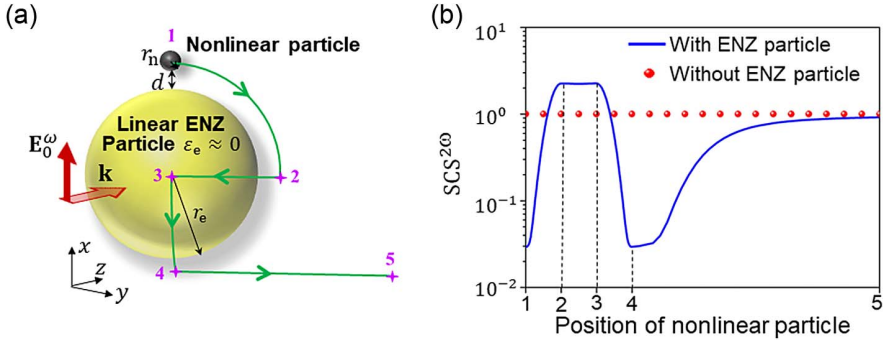

Fig. 2. (a) Schematic layout of the configuration for exploring the SHG quenching effect. It is composed of a linear ENZ spherical particle accompanied with a tiny nonlinear spherical particle in the deep-subwavelength scale. The green curve denotes the trajectory of the nonlinear particle moving around the ENZ particle. Positions 1 and 4 are close to the poles, positions 2 and 3 are on the equatorial plane, and position 5 is far from the ENZ particle. The two particles are illuminated by a plane wave propagating along the z direction with the electric field polarized in the x direction. (b) The blue solid line denotes the normalized scattering cross section of SHG $SCS^{2\omega}$ as a function of the position of the nonlinear particle along the trajectory in (a). The red dots show the $SCS^{2\omega}$ from the nonlinear particle alone, which is normalized to 1.

efficiency of the nonlinear particle. The $SCS^{2\omega}$ reaches the maximal value when the nonlinear particle is on the equatorial plane of the ENZ particle (positions 2 and 3), while it is largely reduced when the nonlinear particle is close to the poles of the ENZ particle (positions 1 and 4). Compared with the case without the ENZ particle, we find that the $SCS^{2\omega}$ from the nonlinear particle at position 1 or 4 is reduced by more than 1 order of magnitude, indicating that the SHG is quenched. Such an SHG quenching effect would fade away if the nonlinear particle is at a distance comparable with the radius of the ENZ particle (position 5), indicating that the quenching of SHG is a short-range effect. The influence of the geometrical parameters on the SHG quenching effect is elaborated in Appendix A.1.

The underlying physics of such a unique position-dependent characteristic lies on the extraordinary evanescent fields near the ENZ particle. When encountering the ENZ particle, the incident light will be scattered into various directions. If the size of the ENZ particle is comparable to or smaller than the wavelength, strong scattered evanescent waves that are evanescent in the forward and backward directions but capable of transferring energy flux along the perpendicular directions would emerge [41–43]. Such evanescent fields vary dramatically with positions, thus leading to the position-dependent SHG efficiency, as observed in Fig. 2. Particularly, near-zero electric field occurs on two sides of the ENZ particle perpendicular to the direction of incidence and along the direction of polarization, which is also denoted as the "side scattering shadows" [41]. When the tiny nonlinear particle is placed there, the incident light cannot "see" it, and therefore the SHG is suppressed.

The generation of the dramatically varying evanescent fields stems from the continuity boundary condition at the ENZ particle–air interface. Since the ENZ particle is at the deep-subwavelength scale, the fundamental electric field inside it can be considered uniform and can be approximately expressed as $\mathbf{E}^{\omega}_{\mathrm{ENZ}} = \frac{3}{2+\varepsilon_e}\mathbf{E}^{\omega}_0$ [43]. Thus, the continuity of the electric displacement field at the poles of the ENZ particle yields

$$\mathbf{E}^{\omega}_{\mathrm{air},p} = \frac{3\varepsilon_e}{2+\varepsilon_e}\mathbf{E}^{\omega}_0, \tag{1}$$

where $\mathbf{E}^{\omega}_{\mathrm{air},p}$ is the electric field at the poles on the air side. On the other hand, the electric field on the equator of ENZ particle on the air side can be obtained as

$$\mathbf{E}^{\omega}_{\mathrm{air},e} = \frac{3}{2+\varepsilon_e}\mathbf{E}^{\omega}_0 \tag{2}$$

due to the continuity of the electric field. When $\varepsilon_e \to 0$, we have

$$\mathbf{E}^{\omega}_{\mathrm{air},e} \gg \mathbf{E}^{\omega}_{\mathrm{air},p} \to 0. \tag{3}$$

Equation (3) indicates the dramatically varying fundamental electric field around the ENZ particle and near-zero electric field at the poles. When a tiny nonlinear particle is placed close to the ENZ particle, it will experience significantly different fundamental electric fields at different positions, thus leading to the position-dependent SHG efficiency. Remarkably, the SHG is quenched when the nonlinear particle is located at the poles as the fundamental electric field there is shielded by the ENZ particle. We note that the extraordinary evanescent fields only exist in the regions very close to the ENZ particle, and therefore the quenching of SHG is a short-range effect.

More strict proof can be obtained based on the Mie scattering theory [44] and the electrostatic theory [45]. Under the limit of $k_0 r_e \ll 1$ (here $k_0 = 2\pi/\lambda_0$), the fundamental electric field outside the ENZ sphere ($r > r_e$) can be derived as (see Appendix A.3 and A.4)

$$\mathbf{E}^{\omega}_{\mathrm{air}} = E^{\omega}_0\left(1 + 2\frac{\varepsilon_e - 1}{\varepsilon_e + 2}\frac{r_e^3}{r^3}\right)\sin\theta\hat{\mathbf{r}} + E^{\omega}_0\left(-1 + \frac{\varepsilon_e - 1}{\varepsilon_e + 2}\frac{r_e^3}{r^3}\right)\cos\theta\hat{\boldsymbol{\theta}}, \tag{4}$$

where r is the distance from the center of the ENZ sphere, and θ is the polar angle (the angle measured from the z axis). When $\varepsilon_e \to 0$, we obtain the amplitude of the fundamental electric field on the ENZ sphere's surface (i.e., $r = r_e$) on the air side as

$$E^{\omega}_{\mathrm{air}} = \frac{3}{2}E^{\omega}_0\cos\theta. \tag{5}$$

Equation (5) implies that the fundamental electric field is enhanced (i.e., $E^{\omega}_{\mathrm{air}} = \frac{3}{2}E^{\omega}_0$) on the equator (i.e., $\theta = 0$), while is zero (i.e., $E^{\omega}_{\mathrm{air}} = 0$) at the poles (i.e., $\theta = \pi/2$), coincident with the above analysis.

For numerical verification, in Fig. 3(a) we show the simulated fundamental electric-field amplitude on the ENZ sphere's surface on the air side in the absence of the nonlinear sphere. The numbers 1–5 represent five different positions corresponding to the positions of the tiny nonlinear sphere in Fig. 2. Apparently, the electric field on the equator (positions 2 and 3) is enhanced compared with that of the incidence, while it is largely reduced to near-zero at the poles (positions 1 and 4). At position 5 which is far away, the influence of the ENZ particle fades away, and the electric field there tends to that of incidence. We note that these extraordinary local electric fields are observed for relatively ideal ENZ particle with $\varepsilon_e = 10^{-4}$. In order to explore the influence of the ε_e on the local electric fields, in Fig. 3(b) we plot the normalized electric-field amplitude $|\mathbf{E}^{\omega}_i|/E^{\omega}_0$ at position i ($i = 1, 2, 3, 4, 5$) as a function of ε_e. We observe that the electric field $|\mathbf{E}^{\omega}_{1,4}|$ (or $|\mathbf{E}^{\omega}_{2,3}|$) decreases (or increases) quickly as the ε_e decreases from unity and becomes stable as long as $\varepsilon_e < 10^{-2}$. Since the evanescent fields only exist very near the ENZ particle, the electric field $|\mathbf{E}^{\omega}_5|$ remains almost unchanged.

We note that the electric field $|\mathbf{E}^{\omega}_{1,4}|$ is not that close to zero because the positions 1 and 4 have a distance of $d = r_e/20$ from the poles of the ENZ sphere. Actually, with reducing d, the $|\mathbf{E}^{\omega}_{1,4}|/E^{\omega}_0$ will tend to be $1.5\varepsilon_e$, as implied in Eq. (1). On the other hand, the $|\mathbf{E}^{\omega}_{2,3}|/E^{\omega}_0$ tends to be 1.5 according to Eq. (2). For verification, in Fig. 3(c) we plot the ratio $|\mathbf{E}^{\omega}_2|/|\mathbf{E}^{\omega}_1|$ with the varying ratio r_e/d (r_e is kept unchanged at $\lambda_0/100$). Here we set $\varepsilon_e = 10^{-4}$. The results clearly show that the ratio $|\mathbf{E}^{\omega}_2|/|\mathbf{E}^{\omega}_1|$ approaches the ideal value (i.e., ε_e^{-1}, red dashed lines) when d is considerably small, consistent with the above theory.

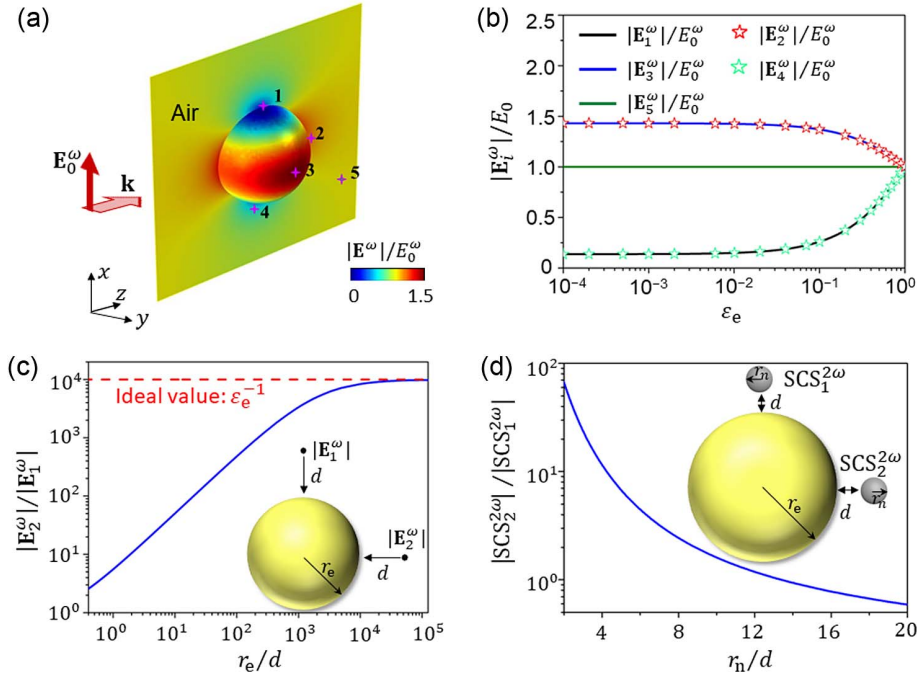

Fig. 3. (a) Distribution of normalized fundamental electric-field amplitude on the ENZ particle's surface on the air side in the absence of the nonlinear particle. The numbers 1–5 denote five different positions of the nonlinear particle in Fig. 2. (b) Normalized fundamental electric-field amplitude $|\mathbf{E}_i^\omega|/E_0^\omega$ at position i ($i = 1, 2, 3, 4, 5$) as a function of the ε_e. (c) The ratio $|\mathbf{E}_2^\omega|/|\mathbf{E}_1^\omega|$ with respect to the ratio r_e/d. Here r_e is kept unchanged at $\lambda_0/100$. The red dashed line shows the ideal value of ε_e^{-1}. The inset illustrates the configuration. (d) The ratio $|SCS_2^{2\omega}|/|SCS_1^{2\omega}|$ with respect to the ratio r_n/d. Here d is kept unchanged at $\lambda_0/2000$. The $SCS_1^{2\omega}$ (or $SCS_2^{2\omega}$) denotes the SHG scattering cross section when the nonlinear particle is placed at position 1 (or 2), as illustrated by the inset.

However, a practical nonlinear particle cannot be infinitely small. The presence of the nonlinear particle could affect the evanescent fields of the ENZ particle. Therefore, the nonlinear particle should be much smaller than the ENZ particle, such that the original evanescent fields are not largely disturbed, and the nonlinear particle can experience enhanced or weakened local fields instead of the averaged fields. In order to show the influence of the particle's size, the ratio of SHG scattering cross section $|SCS_2^{2\omega}|/|SCS_1^{2\omega}|$ as a function of the ratio r_n/d is plotted in Fig. 3(d). Here d is kept unchanged at $\lambda_0/2000$. The $SCS_1^{2\omega}$ (or $SCS_2^{2\omega}$) denotes the SHG scattering cross section when the nonlinear particle is placed at position 1 (or 2), as illustrated by the inset in Fig. 3(d). We see that the ratio $|SCS_2^{2\omega}|/|SCS_1^{2\omega}|$ increases with the reducing r_n, indicating better SHG quenching performance with smaller r_n.

The above results suggest that in order to achieve excellent performance of SHG quenching effect, the conditions of $\varepsilon_e \le 10^{-2}$ and $d \sim r_n \ll r_e$ shall be satisfied. In addition, it is noteworthy that the SHG quenching effect is robust against the material loss of the ENZ particle. We find that even when the ε_e possesses an imaginary part 3 orders of magnitude larger than its real part, the good performance of SHG quenching effect can still be obtained (see Appendix A.2).

3. SHG QUENCHING IN GENERAL SITUATIONS

The extraordinary evanescent waves and the consequent SHG quenching effect are general and could be observed in arbitrary-shaped ENZ particles and anisotropic ENZ particles. As an example, in Fig. 4(a) we present the simulated fundamental electric-field distribution on the surface of a finite-sized isotropic ENZ film ($\varepsilon_e = 10^{-4}$, with dimensions $0.02\lambda_0 \times 0.02\lambda_0 \times 0.005\lambda_0$) on the air side under illumination of a plane wave. Prohibition of electric field above (or below) the cuboid's upper (or lower) surface is clearly observed. Under this circumstance, a tiny nonlinear particle placed above the ENZ film cannot "see" the incident light, and therefore the SHG will be suppressed. For a demonstration, in Fig. 4(b) we compare the normalized SHG scattering cross section $SCS^{2\omega}$ from a nonlinear particle alone (red lines) and that from the nonlinear particle placed above the ENZ film at an edge-to-edge distance of $\lambda_0/2000$ (blue lines) as a function of ε_e. Here the nonlinear particle is the same as that in Fig. 2. It is seen that the $SCS^{2\omega}$ can be reduced by more than 2 orders of magnitude by the ENZ film with $\varepsilon_e \le 10^{-2}$ compared with the $SCS^{2\omega}$ from the nonlinear particle alone, indicating the suppression of SHG by the ENZ cuboid.

Moreover, we consider an anisotropic ENZ film with $\varepsilon_{e,x} = 1$, $\varepsilon_{e,y} = 1$, and $\varepsilon_{e,z} = 10^{-4}$, which are the x, y, and z components of the relative permittivity tensor, respectively. We see from Fig. 4(c) that the prohibition of electric field above (or below) the cuboid's upper (or lower) surface still exists irrespective of the existence of anisotropy. This is because the z component of the electric field on the air side is proportional to $\varepsilon_{e,z}$ and is therefore near zero, as a result of the continuity of the electric displacement field. The SHG quenching effect is

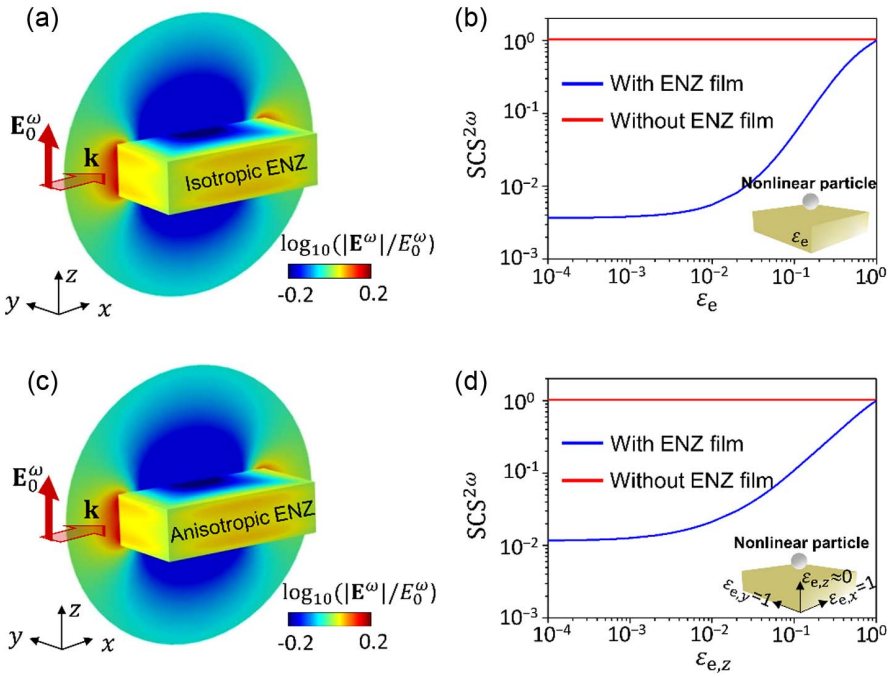

Fig. 4. (a) and (c) Distribution of normalized fundamental electric-field amplitude on the surface of an (a) isotropic, (c) anisotropic ENZ film on the air side in the absence of the nonlinear particle. The incident light is polarized in the z direction and propagates along the x direction. (b) and (d) Normalized $SCS^{2\omega}$ from a nonlinear particle alone (red) and the nonlinear particle placed above the (b) isotropic ENZ film with different ε_e, (d) anisotropic ENZ film with different $\varepsilon_{e,z}$ at an edge-to-edge distance of $\lambda_0/2000$ (blue). The nonlinear particle is the same as that in Fig. 2. The insets illustrate the configurations.

verified in Fig. 4(d). We see that the anisotropic ENZ film with $\varepsilon_{e,z} \leq 10^{-2}$ can significantly reduce the SHG scattering cross section $SCS^{2\omega}$ from the nonlinear particle to near 2 orders of magnitude (blue lines) compared with the $SCS^{2\omega}$ from the nonlinear particle alone (red lines). These results clearly manifest the universality of the SHG quenching effect.

4. DYNAMIC CONTROL OF SHG QUENCHING WITH OPTICAL METASURFACES

The universality of the SHG quenching effect suggests that it could be extended to other systems besides the above particle-scattering system to explore more efficient ways to control the SHG conversion efficiency. In fact, metasurfaces [46–49], as two-dimensional artificial electromagnetic materials structured at the subwavelength scale, provide a versatile platform for manipulating light–matter interactions and realizing significant nonlinear responses [4–6,12,13]. In the following, we would like to show a kind of optical metasurface exhibiting switchable SHG quenching effect.

Figures 5(a) and 5(b) show the schematic graphs of the optical metasurface, consisting of a square array of meta-atoms with a lattice constant of 200 nm on a 2 μm thick silica (SiO_2) substrate. Each meta-atom comprises a large cuboid (100 nm × 100 nm × 50 nm in dimension) accompanied with two small SiO_2 cuboids (20 nm × 20 nm × 25 nm in dimension) on the upper and lower sides, as illustrated by the insets. The top surface of the SiO_2 cuboid is covered by a layer of graphene. In practical realization, such patterned graphene could be fabricated through photolithography [50], electron beam lithography [51], plasma etching [52], laser direct patterning [53], etc. The graphene is known as a unique nonlinear optical material with outstanding optical properties [13,54–56]. Generally, the SHG is forbidden of free-standing graphene due to its centrosymmetry. Interestingly, when the graphene is placed on a substrate with broken inversion symmetry (e.g., the SiO_2 utilized here), SHG would be allowed [13]. Considering the fact that graphene belongs to the D_{6h} symmetry group, its surface second-order nonlinear optical conductivity tensor $\overleftrightarrow{\sigma}^{(2)}$ only has three independent nonzero components, i.e., $\sigma^{(2)}_{\perp\perp\perp}$, $\sigma^{(2)}_{\parallel\parallel\perp} = \sigma^{(2)}_{\parallel\perp\parallel}$, and $\sigma^{(2)}_{\perp\parallel\parallel}$ [13,57,58]. Here, we set $\chi^{(2)}_{\perp\perp\perp} = \frac{i}{2\omega\varepsilon_0 h_{\text{eff}}}\sigma^{(2)}_{\perp\perp\perp}$, $\chi^{(2)}_{\perp\parallel\parallel} = \frac{i}{2\omega\varepsilon_0 h_{\text{eff}}}\sigma^{(2)}_{\perp\parallel\parallel}$, and $\chi^{(2)}_{\parallel\parallel\perp} = \frac{i}{2\omega\varepsilon_0 h_{\text{eff}}}\sigma^{(2)}_{\parallel\parallel\perp}$, where $\sigma^{(2)}_{\perp\perp\perp} = -9.71i \times 10^{-16}$ AmV^{-2}, $\sigma^{(2)}_{\perp\parallel\parallel} = -2.09i \times 10^{-16}$ AmV^{-2}, $\sigma^{(2)}_{\parallel\parallel\perp} = -2.56i \times 10^{-16}$ AmV^{-2}, and $h_{\text{eff}} = 0.33$ nm is the effective thickness of graphene [13].

The central large cuboid is composed of eight alternative layers of semiconductor CdO and phase-change material GeTe. The thickness of each CdO (or GeTe) layer is $t_{\text{CdO}} = 13.1$ nm (or $t_{\text{GeTe}} = 11.9$ nm). The relative permittivity of CdO can be described using the Drude model as $\varepsilon_{\text{CdO}} = \varepsilon_\infty - \frac{\omega_p^2}{\omega(\omega+i\gamma)}$ [59], where $\varepsilon_\infty = 5.5$, $\omega_p = 1.23 \times 10^{15}$ rad/s, and $\gamma = 1.77 \times 10^{13}$ rad/s. The GeTe possesses the ability of rapidly switching between the crystalline and amorphous phases in a reversible way, and the phase transition can be achieved optically or through Joule heating and is proven to be reliable, fast, and repeatable [60,61]. Remarkably, the optical properties of GeTe in different phases are

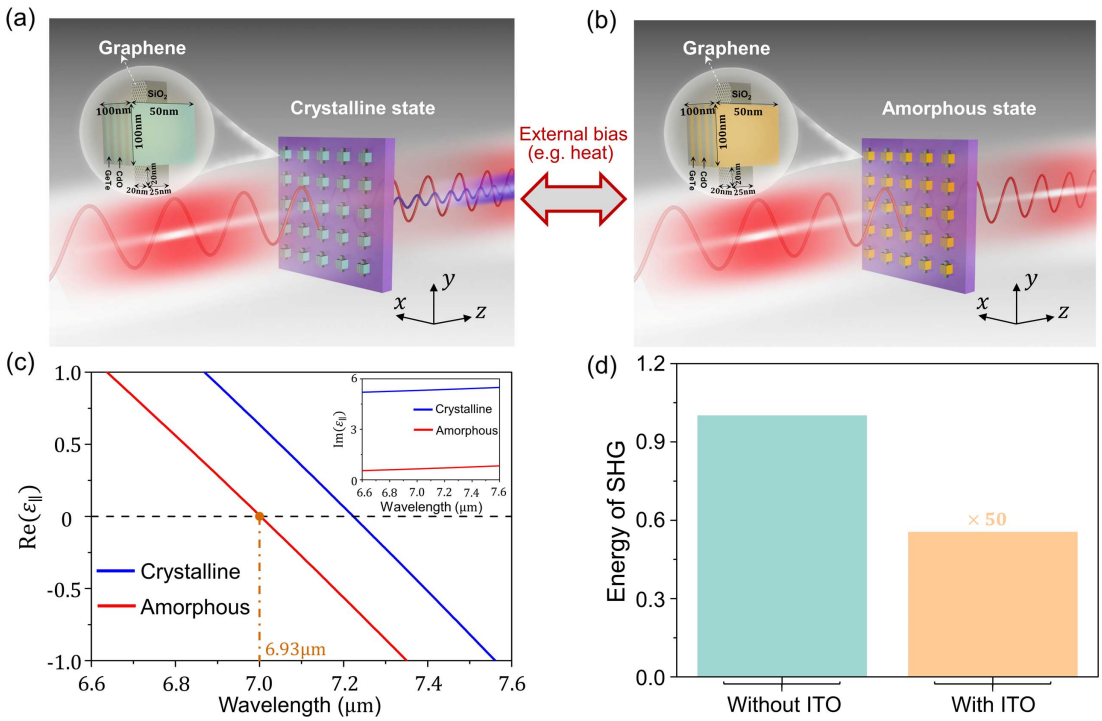

Fig. 5. (a) and (b) Schematic graphs of an optical metasurface which can be dynamically switched to exhibit (a) high, (b) low SHG conversion efficiency through controlling the phase states of its constituent GeTe. The metasurface is composed of a square array of meta-atoms on a SiO_2 substrate. Each meta-atom consists of a central CdO–GeTe multilayered structure and two small graphene-covered SiO_2 cuboids, as illustrated by the insets. The length unit is nanometer. (c) The real part of $\varepsilon_{y,\mathrm{eff}}$, i.e., $\mathrm{Re}(\varepsilon_{y,\mathrm{eff}})$, of the central CdO–GeTe multilayer with GeTe in the crystalline (blue) or amorphous (red) phase as a function of wavelength. The inset shows the imaginary part of $\varepsilon_{y,\mathrm{eff}}$, i.e., $\mathrm{Im}(\varepsilon_{y,\mathrm{eff}})$. (d) The SHG energy from the metasurface with its constituent GeTe in the crystalline (green) or amorphous (yellow) phase. The SHG energy in the amorphous phase is enlarged by 10 times for better visualization. In each phase, the left and right bars correspond to the case with the central CdO–GeTe multilayer considered as an effective medium and the case with the original multilayer structure, respectively. The incident light is polarized in the y direction and propagates along the z direction. The operating wavelength is 6.93 μm.

significantly different, and thus the optical properties of the CdO–GeTe multilayer can be efficiently manipulated through changing the phase states of GeTe. Due to the deep-subwavelength size, the CdO–GeTe multilayer can be approximately homogenized as an effective anisotropic medium, whose y component of effective relative permittivity can be expressed as $\varepsilon_{y,\mathrm{eff}} = (\varepsilon_{\mathrm{CdO}} t_{\mathrm{CdO}} + \varepsilon_{\mathrm{GeTe}} t_{\mathrm{GeTe}})/(t_{\mathrm{CdO}} + t_{\mathrm{GeTe}})$ [62]. In Fig. 5(c), we plot the real part of $\varepsilon_{y,\mathrm{eff}}$, i.e., $\mathrm{Re}(\varepsilon_{y,\mathrm{eff}})$, as a function of wavelength when the GeTe is in the crystalline (blue lines) or the amorphous (red lines) phase. We see that $\mathrm{Re}(\varepsilon_{y,\mathrm{eff}}) = 0$ at the wavelength of 6.93 μm in the amorphous phase, in which case the imaginary part of $\varepsilon_{y,\mathrm{eff}}$, i.e., $\mathrm{Im}(\varepsilon_{y,\mathrm{eff}})$, is not very large (see the inset). Under this circumstance, the central CdO–GeTe multilayer in the amorphous phase can be viewed as an effective anisotropic ENZ medium with $\varepsilon_{y,\mathrm{eff}} \approx 0$. However, when the GeTe is switched to the crystalline phase, we have $\mathrm{Re}(\varepsilon_{y,\mathrm{eff}}) = 0.81 \gg 0$ and $\mathrm{Im}(\varepsilon_{y,\mathrm{eff}}) = 5.29$, indicating the breakdown of the ENZ condition.

This unique property provides us with a route to dynamically control the occurrence and quenching of SHG of the optical metasurface through switching the phases of GeTe, as schematically shown in Figs. 5(a) and 5(b). When the GeTe is in the amorphous phase, the CdO–GeTe multilayer effectively serves as an anisotropic ENZ medium, which can generate near-zero local electric fields near the surfaces normal to the y direction (see field distributions in Appendix A.5). The graphene placed there will be hard to "see" the incident light, and therefore the SHG from the graphene is suppressed [Fig. 5(b)]. Interestingly, when the GeTe is switched to the crystalline phase, the ENZ condition breaks down, and the SHG from the graphene emerges [Fig. 5(a)].

For numerical verification, we set the relevant parameters of graphene as $\sigma^{(2)}_{\perp\perp\perp} = -9.71i \times 10^{-16}$ $\mathrm{AmV^{-2}}$, $\sigma^{(2)}_{\parallel\parallel\perp} = \sigma^{(2)}_{\parallel\perp\parallel} = -2.56i \times 10^{-16}$ $\mathrm{AmV^{-2}}$, and $\sigma^{(2)}_{\perp\parallel\parallel} = -2.09i \times 10^{-16}$ $\mathrm{AmV^{-2}}$ at the operating wavelength of 6.93 μm [13]. At this wavelength, the second-order nonlinear susceptibility of graphene ($\sim 10^{-10}$ m/V) is several orders of magnitude larger than those of CdO ($\sim 10^{-18}$ m/V) [22], GeTe ($\sim 10^{-18}$ m/V) [63], and SiO_2 [13], and therefore, here we consider the nonlinear responses of graphene only. In practical implementations, the graphene can be replaced by other optical materials with large nonlinear susceptibility such as gallium arsenide [64]. Figure 5(d) presents the SHG energy from the metasurface with GeTe in the crystalline (green bars) or amorphous (yellow bars) phase under illumination of normally incident light (polarized in the y direction). In each phase, the left and right

bars correspond to the case with the central CdO–GeTe multilayer considered as an effective medium and the case with the original multilayered structure, respectively, showing good agreement. We note that the SHG energy in the amorphous phase is enlarged by 10 times for better visualization. We see that the SHG energy in the amorphous phase is much lower than that in the crystalline phase, demonstrating the dynamically controllable SHG quenching effect in the optical metasurface.

We note that the pump laser used to enhance the SHG of graphene generally will not inadvertently change the phase of GeTe for two reasons. First, the intensity of the laser pulse that can effectively enhance the SHG of graphene is generally lower than that required to change the phase of GeTe because the transition temperature of GeTe is high [65,66]. Second, the activation energy of GeTe is ∼3.14 eV [67]. This indicates that the wavelength of the laser pulse used to change the phase of GeTe is required to be short, e.g., ∼248 nm [65,67], much shorter than the operating wavelength for SHG quenching (i.e., 6.93 μm).

In practical implementation, the constituent materials of the metasurface can be flexibly chosen. For example, graphene could be replaced by other two-dimensional materials with pronounced nonlinear optical properties, such as transition metal dichalcogenides (TMDs) including MoS_2, WS_2, and $MoSe_2$ [68,69]. The CdO–GeTe composite could be replaced by other materials such as indium tin oxide, aluminum-doped zinc oxide, and metal–dielectric composites operating at the ENZ frequency [70,71], but the drawback is that the ENZ wavelength cannot be dynamically controlled.

5. DISCUSSION AND CONCLUSION

The SHG conversion efficiency of a nonlinear material strongly depends on its molecular-scale constituents and their macroscopic ordering [8]. Based on this property, a conventional approach to manipulate the SHG signal is to engineer the local and global symmetries of meta-atoms in metamaterials and metasurfaces [72–74]. In addition, the enhancement of SHG due to surface plasmon polariton resonance in metallic nanostructures is very sensitive to each meta-atom's geometry, dielectric environment, and polarization of incidence, thus providing another approach to manipulate the SHG signal [75,76]. Here, unlike the previous endeavors, our approach paves a route to control the SHG conversion efficiency through exploiting the near-field effect of a linear material [77], that is, the extraordinary local fundamental electric fields of an ENZ particle, thus further realizing the unique SHG quenching effect. Our approach could be extended to other nonlinear optical processes, including sum- and difference-frequency generation.

It is noteworthy that TMDs, such as MoS_2, WS_2, and $MoSe_2$, are capable of controlling the SHG conversion efficiency [68,69]. Due to their unique electronic band structures and strong light–matter interactions at the atomic scale, the SHG process of TMDs is sensitive to the number of layers, crystallinity, and interlayer coupling in TMD heterostructures [68,69,78–81]. Interestingly, it was demonstrated that the SHG is quenched in even layered MoS_2 as it belongs to the centrosymmetric D_{3d} space group [78,79]. Fundamentally different from the SHG quenching with TMDs, the SHG quenching by the ENZ media attributes to the macroscopic electromagnetic responses.

Our findings could have an impact on the experimental investigations of optical nonlinearity with ENZ media. A frequently used configuration in experiments is to exploit plasmonic or dielectric nanoantennas placed on a thin ENZ film [25,27–30,37]. Usually, the boost of nonlinear responses induced by the large field enhancement in the ENZ film is reported. Nevertheless, our results in Fig. 4 indicate that the thin ENZ film could significantly suppress the nonlinear responses from the nanoantennas. This breaks the traditional conception that the ENZ media are always responsible for SHG enhancement and enriches the understanding of the experimental observation of optical nonlinearity.

In conclusion, we have demonstrated the SHG quenching effect when a tiny nonlinear particle is placed very close to a subwavelength ENZ particle. The SHG quenching effect is found to originate from the extraordinary near-zero local electric fields occurring near the ENZ particle due to evanescent scattering waves and is proved to be universal with both isotropic and anisotropic ENZ particles, irrespective of their shapes. Based on the principle of SHG quenching effect, we have further demonstrated a kind of dynamically controllable optical metasurface integrated with phase-change material GeTe. Through changing the phase states of GeTe, the SHG from the metasurface can be switched on or off. Our work creates pathways for applications such as nonlinear optical switches and modulators based on the integration of nonlinear materials and ENZ media.

APPENDIX A

1. Influence of Geometrical Parameters

In Fig. 6, we investigate the influence of geometrical parameters, that is, particles' radii r_e and r_n, and the edge-to-edge distance d on the SHG quenching effect. The model is adopted from Fig. 2. The tiny nonlinear particle is placed at position 1 where the SHG quenching effect is expected, as illustrated in Fig. 6(a). We see from Fig. 6(b) that the SHG $SCS^{2\omega}$ decreases with increasing r_e, because the region of electric-field suppression becomes larger, and the fundamental electric field experienced by the tiny nonlinear particle becomes smaller. This indicates that we can obtain better performance of SHG quenching effect when using relatively large ENZ particles. From Figs. 6(c) and 6(d), we see that the SHG $SCS^{2\omega}$ increases with the increasing radius of the tiny nonlinear particle r_n and the edge-to-edge distance d. As we have demonstrated above, the quenching of SHG is a short-range effect, and the near-zero fundamental electric fields appear at the poles of the ENZ particle. Therefore, a nonlinear particle with large r_n would experience averaged fields instead of the greatly weakened local fields at the poles of the ENZ particle. On the other hand, the nonlinear particle far way (i.e., d is large) would not "see" the greatly weakened local fields at the poles. As a consequence, the SHG quenching effect would fade away if the nonlinear particle is large or far away from the poles of the ENZ particle.

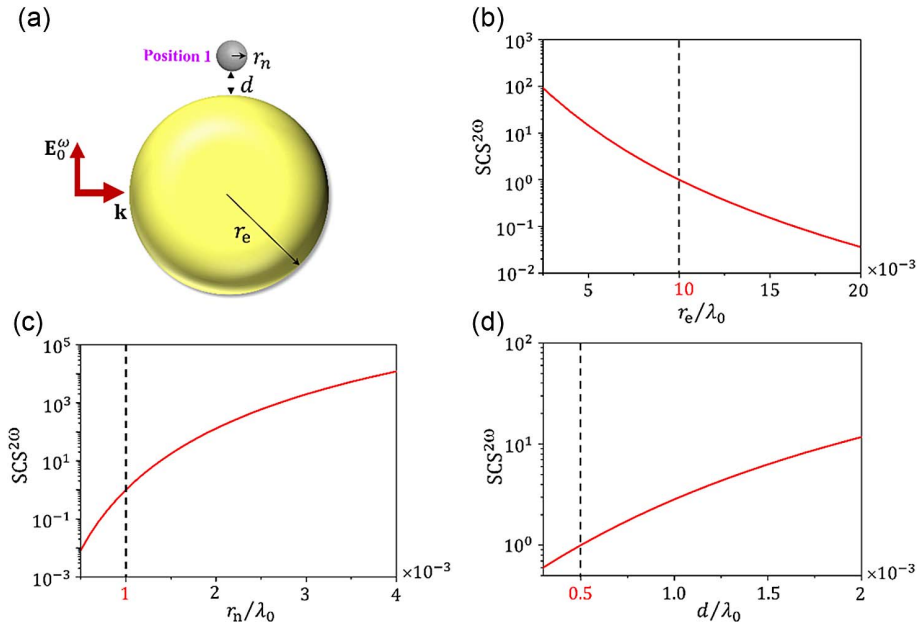

Fig. 6. (a) Schematic layout of the configuration, which is the same as that in Fig. 2 in the main text. Here, the tiny nonlinear particle is placed at position 1 where the SHG quenching effect is expected. (b)–(d) Normalized SHG scattering cross section $SCS^{2\omega}$ with respect to the (b) r_e/λ_0 in the case of $r_n/\lambda_0 = 0.001$ and $d/\lambda_0 = 0.0005$, (c) r_n/λ_0 in the case of $r_e/\lambda_0 = 0.01$ and $d/\lambda_0 = 0.0005$, and (d) d/λ_0 in the case of $r_e/\lambda_0 = 0.01$ and $r_n/\lambda_0 = 0.001$. In (b)–(d), the $SCS^{2\omega}$ is normalized to the $SCS^{2\omega}$ in Fig. 2, in which case the geometrical parameters are set as $r_e/\lambda_0 = 0.01$, $r_n/\lambda_0 = 0.001$, and $d/\lambda_0 = 0.0005$ (marked by the vertical dashed lines).

In short, to obtain better performance of SHG quenching effect, the radius of the nonlinear particle should be much smaller than that of the ENZ particle, and the distance between the two particles should be as small as possible. Based on this understanding, we set the geometrical parameters of the model in Fig. 2 as $r_e/\lambda_0 = 0.01$, $r_n/\lambda_0 = 0.001$, and $d/\lambda_0 = 0.0005$ (marked by the vertical dashed lines).

2. Influence of Material Losses

Figure 7 discusses the influence of material losses of the ENZ particle on the SHG quenching effect. The configuration is the same as that in Fig. 2. Figure 7(a) shows the scattering cross section of SHG $SCS^{2\omega}$ from the tiny nonlinear particle when it is successively moved from position 1 to position 5 along the trajectory $1 \to 2 \to 3 \to 4 \to 5$ [green curves in Fig. 2(a)]. The red dots are related to the case without the ENZ particle. The blue lines correspond to the case with a lossless ENZ particle of $\varepsilon_e = 10^{-4}$ (the same as that in Fig. 2), and the star markers correspond to the case with a lossy ENZ particle of $\varepsilon_e = 10^{-4} + 10^{-3}i$ (purple) or $\varepsilon_e = 10^{-4} + 10^{-2}i$ (yellow) or $\varepsilon_e = 10^{-4} + 10^{-1}i$ (green). The results show that even when the ε_e possesses an imaginary part 3 orders of magnitude larger than its real part, the SHG conversion efficiency is almost unchanged, and the good performance of SHG quenching can still be obtained. This is because the material losses have little influence on the near-zero local electric fields at the poles of the ENZ particle. For verification, in Figs. 7(b)–7(d) we plot the simulated fundamental electric-field amplitude on the ENZ sphere's surface on the air side for the cases with material losses. Clearly, the field distributions are almost unchanged in the presence of material losses.

3. Derivation of Field Distributions Based on MIE Scattering Theory

Here, we consider an ENZ spherical particle in air (relative permittivity ε_e, relative permeability μ_e, radius r_e) illuminated by a plane wave. According to Mie scattering theory, we can obtain the electric fields of incidence, the scattered waves, and the waves inside the particle. The electric fields inside the particle:

$$\begin{cases} E_{e,r}^{\omega} = \frac{E_0}{k_e^2}\sum_{n=1}^{\infty} i^{n-1}\frac{2n+1}{n(n+1)}\left(F_n^{\mathrm{TM}}\frac{\partial^2\psi_n(k_e r)}{\partial r^2} + k_e^2 F_n^{\mathrm{TM}}\psi_n(k_e r)\right)P_n^{(1)}(\cos\theta)\cos\theta \\ E_{e,\theta}^{\omega} = \frac{1}{r}\frac{E_0}{k_e^2}\sum_{n=1}^{\infty} i^{n-1}\frac{2n+1}{n(n+1)}\left(F_n^{\mathrm{TM}}\frac{\partial\psi_n(k_e r)}{\partial r}\frac{\partial P_n^{(1)}(\cos\theta)}{\partial\theta} + ik_e F_n^{\mathrm{TE}}\psi_n(k_e r)\frac{P_n^{(1)}(\cos\theta)}{\sin\theta}\right)\cos\varphi \\ E_{e,\varphi}^{\omega} = -\frac{1}{r}\frac{E_0}{k_e^2}\sum_{n=1}^{\infty} i^{n-1}\frac{2n+1}{n(n+1)}\left(F_n^{\mathrm{TM}}\frac{\partial\psi_n(k_e r)}{\partial r}\frac{P_n^{(1)}(\cos\theta)}{\sin\theta} + ik_e F_n^{\mathrm{TE}}\psi_n(k_e r)\frac{\partial P_n^{(1)}(\cos\theta)}{\partial\theta}\right)\sin\varphi \end{cases}. \quad \text{(A1a)}$$

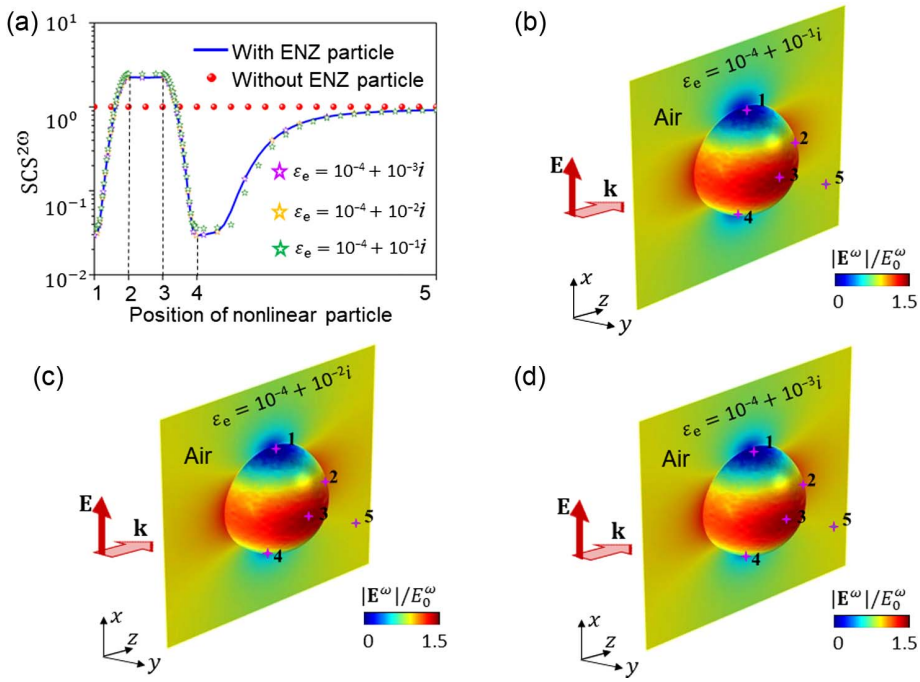

Fig. 7. (a) Normalized scattering cross section of SHG SCS$^{2\omega}$ from the tiny nonlinear particle when it is successively moved from position 1 to position 5 along the trajectory $1 \to 2 \to 3 \to 4 \to 5$. The configuration is the same as that in Fig. 2. (b)–(d) Simulated fundamental electric-field amplitude on the ENZ sphere's surface on the air side for the cases with material losses.

The electric fields of incidence:

$$\begin{cases} E_{\mathrm{in},r}^{\omega} = \frac{E_0}{k_0^2}\sum_{n=1}^{\infty} i^{n-1}\frac{2n+1}{n(n+1)}\left(\frac{\partial^2\psi_n(k_0r)}{\partial r^2} + k_0^2\psi_n(k_0r)\right)P_n^{(1)}(\cos\theta)\cos\varphi \\ E_{\mathrm{in},\theta}^{\omega} = \frac{1}{r}\frac{E_0}{k_0^2}\sum_{n=1}^{\infty} i^{n-1}\frac{2n+1}{n(n+1)}\left(\frac{\partial\psi_n(k_0r)}{\partial r}\frac{\partial P_n^{(1)}(\cos\theta)}{\partial\theta} + ik_0\psi_n(k_0r)\frac{P_n^{(1)}(\cos\theta)}{\sin\theta}\right)\cos\varphi \\ E_{\mathrm{in},\varphi}^{\omega} = -\frac{1}{r}\frac{E_0}{k_0^2}\sum_{n=1}^{\infty} i^{n-1}\frac{2n+1}{n(n+1)}\left(\frac{\partial\psi_n(k_0r)}{\partial r}\frac{P_n^{(1)}(\cos\theta)}{\sin\theta} + ik_0\psi_n(k_0r)\frac{\partial P_n^{(1)}(\cos\theta)}{\partial\theta}\right)\sin\varphi \end{cases} \quad \textbf{(A1b)}$$

The electric fields of scattered waves:

$$\begin{cases} E_{\mathrm{sc},r}^{\omega} = \frac{E_0}{k_0^2}\sum_{n=1}^{\infty} i^{n-1}\frac{2n+1}{n(n+1)}\left(A_n^{\mathrm{TM}}\frac{\partial^2\varsigma_n^{(1)}(k_0r)}{\partial r^2} + k_0^2A_n^{\mathrm{TM}}\varsigma_n^{(1)}(k_0r)\right)P_n^{(1)}(\cos\theta)\cos\varphi \\ E_{\mathrm{sc},\theta}^{\omega} = \frac{1}{r}\frac{E_0}{k_0^2}\sum_{n=1}^{\infty} i^{n-1}\frac{2n+1}{n(n+1)}\left(A_n^{\mathrm{TM}}\frac{\partial\varsigma_n^{(1)}(k_0r)}{\partial r}\frac{\partial P_n^{(1)}(\cos\theta)}{\partial\theta} + ik_0A_n^{\mathrm{TE}}\varsigma_n^{(1)}(k_0r)\frac{P_n^{(1)}(\cos\theta)}{\sin\theta}\right)\cos\varphi \\ E_{\mathrm{sc},\varphi}^{\omega} = -\frac{1}{r}\frac{E_0}{k_0^2}\sum_{n=1}^{\infty} i^{n-1}\frac{2n+1}{n(n+1)}\left(A_n^{\mathrm{TM}}\frac{\partial\varsigma_n^{(1)}(k_0r)}{\partial r}\frac{P_n^{(1)}(\cos\theta)}{\sin\theta} + ik_0A_n^{\mathrm{TE}}\varsigma_n^{(1)}(k_0r)\frac{\partial P_n^{(1)}(\cos\theta)}{\partial\theta}\right)\sin\varphi \end{cases} \quad \textbf{(A1c)}$$

Combining the boundary conditions at $r = r_e$

$$\mathbf{e}_r \times (\mathbf{E}_{\mathrm{in}}^{\omega} + \mathbf{E}_{\mathrm{sc}}^{\omega}) = \mathbf{e}_r \times \mathbf{E}_e^{\omega}, \qquad \mathbf{e}_r \times (\mathbf{H}_{\mathrm{in}}^{\omega} + \mathbf{H}_{\mathrm{sc}}^{\omega}) = \mathbf{e}_r \times \mathbf{H}_e^{\omega}, \quad \textbf{(A2)}$$

we obtain the coefficients F_n^{TM}, F_n^{TE}, A_n^{TM}, and A_n^{TE} as

$$F_n^{\mathrm{TM}} = \frac{\varepsilon_e\psi_n(k_0r_e)\varsigma_n^{(1)\prime}(k_0r_e) - \varepsilon_e\varsigma_n^{(1)}(k_0r_e)\psi_n'(k_0r_e)}{\sqrt{\varepsilon_e}\psi_n(k_er_e)\varsigma_n^{(1)\prime}(k_0r_e) - \varsigma_n^{(1)}(k_0r_e)\psi_n'(k_er_e)}, \quad \textbf{(A3a)}$$

$$F_n^{\mathrm{TE}} = \frac{\sqrt{\varepsilon_e}\psi_n'(k_0r_e)\varsigma_n^{(1)}(k_0r_e) - \sqrt{\varepsilon_e}\varsigma_n^{(1)\prime}(k_0r_e)\psi_n(k_0r_e)}{\psi_n'(k_er_e)\varsigma_n^{(1)}(k_0r_e) - \varsigma_n^{(1)\prime}(k_0r_e)\psi_n(k_er_e)}, \quad \textbf{(A3b)}$$

$$A_n^{\mathrm{TM}} = \frac{\psi_n'(k_er_e)\psi_n(k_0r_e) - \sqrt{\varepsilon_e}\psi_n(k_er_e)\psi_n'(k_0r_e)}{\sqrt{\varepsilon_e}\psi_n(k_er_e)\varsigma_n^{(1)\prime}(k_0r_e) - \varsigma_n^{(1)}(k_0R_0)\psi_n'(k_er_e)}, \quad \textbf{(A3c)}$$

$$A_n^{\mathrm{TE}} = \frac{\psi_n(k_e r_e)\psi_n'(k_0 r_e) - \psi_n'(k_e r_e)\psi_n(k_0 r_e)}{\psi_n'(k_e r_e)\varsigma_n^{(1)}(k_0 r_e) - \varsigma_n^{(1)\prime}(k_0 r_e)\psi_n(k_e r_e)}. \quad \textbf{(A3d)}$$

Here, we assume that the ENZ particle's size is much smaller than the wavelength (i.e., $k_0 r_e \ll 1$). In this situation, the terms other than the dipolar term (i.e., $n = 1$) can be neglected. Then the coefficients A_n^{TM} and A_n^{TE} can be simplified to $A_1^{\mathrm{TM}} \to -\psi_1(k_0 r_e)/\varsigma_1^{(1)}(k_0 r_e)$ and $A_1^{\mathrm{TE}} \to 0$ under the limit of $\varepsilon_e \to 0$. Thus, the electric field outside the particle $\mathbf{E}_{\mathrm{air}}^{\omega} = \mathbf{E}_{\mathrm{in}}^{\omega} + \mathbf{E}_{\mathrm{sc}}^{\omega}$ can be simplified to

$$|\mathbf{E}_{\mathrm{air}}^{\omega}| = \frac{3}{2} E_0 \cos\theta, \quad \textbf{(A4)}$$

where θ is the polar angle. Equation (A4) indicates enhanced fundamental electric field (i.e., $E_{\mathrm{air}}^{\omega} = \frac{3}{2}E_0^{\omega}$) on the equator (i.e., $\theta = 0$), while zero fundamental electric field (i.e., $E_{\mathrm{air}}^{\omega} = 0$) at the poles (i.e., $\theta = \pi/2$).

4. Derivation of Field Distributions Based on Electrostatic Theory

Since the ENZ particle is at the deep-subwavelength scale, we can also derive the electric field distributions based on electrostatic theory. In the electrostatic theory, the electric field satisfies the Laplace equation $\nabla \cdot \nabla\phi(r,\theta) = 0$ with $\mathbf{E} = -\nabla\phi$. By solving the Laplace equation, the general expressions for the electric potentials can be written as

$$\phi_e^{\omega} = BE_0 r \sin\theta, \qquad r \le r_e, \quad \textbf{(A5a)}$$

$$\phi_{\mathrm{air}}^{\omega} = \left(-r + \frac{C}{r^2}\right) E_0 \sin\theta, \qquad r > r_e, \quad \textbf{(A5b)}$$

where B and C are unknown coefficients to be determined. Then the electric fields in different regions can be calculated as

$$\mathbf{E}_e^{\omega} = BE_0(\sin\theta \mathbf{e}_r - \cos\theta \mathbf{e}_\theta), \qquad r \le r_e, \quad \textbf{(A6a)}$$

$$\mathbf{E}_{\mathrm{air}}^{\omega} = \left(1 + \frac{C}{r^3}\right) E_0 \sin\theta \mathbf{e}_r - \left(1 - \frac{C}{r^3}\right) E_0 \cos\theta \mathbf{e}_\theta, \qquad r > r_e. \quad \textbf{(A6b)}$$

Considering the boundary conditions at $r = r_e$, we have

$$\mathbf{e}_r \times (\mathbf{E}_{\mathrm{air}}^{\omega} - \mathbf{E}_e^{\omega}) = 0, \qquad \mathbf{e}_r \cdot (\mathbf{D}_{\mathrm{air}}^{\omega} - \mathbf{D}_e^{\omega}) = 0. \quad \textbf{(A7)}$$

Based on Eq. (A7), the expressions of the coefficients B and C can be obtained. Inserting them into Eq. (A6), the electric fields in different regions can be expressed as

$$\mathbf{E}_e^{\omega} = \frac{3E_0}{\varepsilon_e + 2}(\sin\theta \mathbf{e}_r - \cos\theta \mathbf{e}_\theta), \qquad r \le r_e, \quad \textbf{(A8a)}$$

$$\mathbf{E}_{\mathrm{air}}^{\omega} = \left(1 + 2\frac{r_e^3(\varepsilon_e - 1)}{r^3(\varepsilon_e + 2)}\right) E_0 \sin\theta \mathbf{e}_r + \left(-1 + \frac{r_e^3(\varepsilon_e - 1)}{r^3(\varepsilon_e + 2)}\right) E_0 \cos\theta \mathbf{e}_\theta, \qquad r > r_e. \quad \textbf{(A8b)}$$

From Eq. (A8), the electric field on the ENZ particle's surface (i.e., $r = r_e$) on the air side can be simplified to

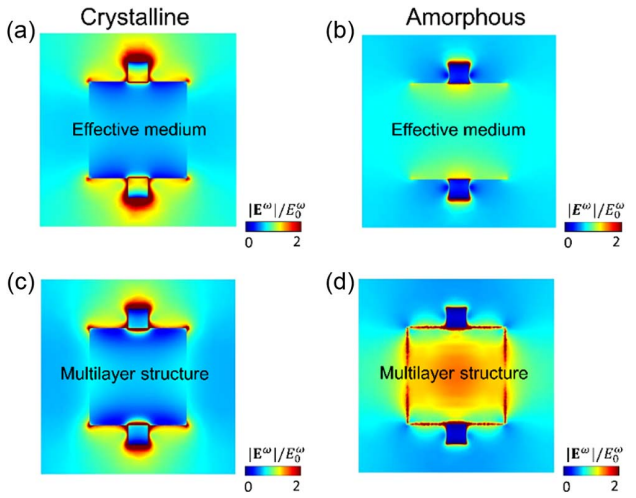

Fig. 8. Distributions of normalized fundamental electric-field amplitude in one unit cell of the optical metasurface on the plane that contains the graphene. The metasurface is the same as that in Fig. 5. (a) Effective-medium model in the crystalline phase; (b) effective-medium model in the amorphous phase; (c) multilayer-structure model in the crystalline phase; and (d) multilayer-structure model in the amorphous phase.

$$\mathbf{E}_{\mathrm{air}}^{\omega} = \frac{3\varepsilon_e}{(\varepsilon_e + 2)} E_0 \sin\theta \mathbf{e}_r - \frac{3}{(\varepsilon_e + 2)} E_0 \cos\theta \mathbf{e}_\theta. \quad \textbf{(A9)}$$

Considering the condition of $\varepsilon_e \to 0$, we obtain the fundamental electric field on the ENZ sphere's surface on the air side as

$$|\mathbf{E}_{\mathrm{air}}^{\omega}| = \frac{3}{2} E_0 \cos\theta. \quad \textbf{(A10)}$$

We see that Eq. (A10) based on the electrostatic theory is the same as Eq. (A4) based on the Mie scattering theory.

5. Field Distributions in Optical Metasurface

Figure 8 supplies the distributions of normalized fundamental electric-field amplitude (on the plane that contains the graphene) in one unit cell of the optical metasurface discussed in Fig. 5. We observe that the field distributions in the effective-medium model and the multilayer-structure model agree well, both showing that the fundamental electric field in the graphene region (upper and lower square areas) in the amorphous phase is much smaller than that in the crystalline phase. This finally leads to much lower SHG conversion efficiency in the amorphous phase, as we have demonstrated in Fig. 5.

Funding. National Natural Science Foundation of China (12174281, 12274314, 92050104); Natural Science Foundation of Jiangsu Province (BK20221240, BK20221354); Suzhou Prospective Application Research Project (SYG202039); Ministry of Science and Higher Education of the Russian Federation (075-15-2022-1150).

Acknowledgment. The authors sincerely thank Professor Yun Lai at Nanjing University for the insights he offered in discussions.

Disclosures. The authors declare no conflicts of interest.

Data Availability. The data that support the findings of this study are available from the corresponding authors upon reasonable request.

REFERENCES

1. M. Kauranen and A. V. Zayats, "Nonlinear plasmonics," Nat. Photonics **6**, 737–748 (2012).
2. N. M. Litchinitser, "Nonlinear optics in metamaterials," Adv. Phys. X **3**, 1367628 (2018).
3. D. Smirnova and Y. S. Kivshar, "Multipolar nonlinear nanophotonics," Optica **3**, 1241–1255 (2016).
4. A. E. Minovich, A. E. Miroshnichenko, A. Y. Bykov, T. V. Murzina, D. N. Neshev, and Y. S. Kivshar, "Functional and nonlinear optical metasurfaces," Laser Photonics Rev. **9**, 195–213 (2015).
5. G. Li, S. Zhang, and T. Zentgraf, "Nonlinear photonic metasurfaces," Nat. Rev. Mater. **2**, 17010 (2017).
6. A. Krasnok, M. Tymchenko, and A. Alù, "Nonlinear metasurfaces: a paradigm shift in nonlinear optics," Mater. Today **21**, 8–21 (2018).
7. O. Reshef, I. De Leon, M. Z. Alam, and R. W. Boyd, "Nonlinear optical effects in epsilon-near-zero media," Nat. Rev. Mater. **4**, 535–551 (2019).
8. J. Butet, P. Brevet, and O. J. F. Martin, "Optical second harmonic generation in plasmonic nanostructures: from fundamental principles to advanced applications," ACS Nano **9**, 10545–10562 (2015).
9. K. Thyagarajan, J. Butet, and O. J. F. Martin, "Augmenting second harmonic generation using Fano resonances in plasmonic systems," Nano Lett. **13**, 1847–1851 (2013).
10. M. Timofeeva, L. Lang, F. Timpu, C. Renaut, A. Bouravleuv, I. Shtrom, G. Cirlin, and R. Grange, "Anapoles in free-standing III-V nanodisks enhancing second-harmonic generation," Nano Lett. **18**, 3695–3702 (2018).
11. Y. Li, Z. Huang, Z. Sui, H. Chen, X. Zhang, W. Huang, H. Guan, W. Qiu, J. Dong, W. Zhu, J. Yu, H. Lu, and Z. Chen, "Optical anapole mode in nanostructured lithium niobate for enhancing second harmonic generation," Nanophotonics **9**, 3575–3585 (2020).
12. A. P. Anthur, H. Zhang, R. Paniagua-Dominguez, D. A. Kalashnikov, S. T. Ha, T. W. W. Maß, A. I. Kuznetsov, and L. Krivitsky, "Continuous wave second harmonic generation enabled by quasi-bound-states in the continuum on gallium phosphide metasurfaces," Nano Lett. **20**, 8745–8751 (2020).
13. Q. Ren, J. W. You, and N. C. Panoiu, "Large enhancement of the effective second-order nonlinearity in graphene metasurfaces," Phys. Rev. B **99**, 205404 (2019).
14. I. Liberal and N. Engheta, "Near-zero refractive index photonics," Nat. Photonics **11**, 149–158 (2017).
15. X. Niu, X. Hu, S. Chu, and Q. Gong, "Epsilon-near-zero photonics: a new platform for integrated devices," Adv. Opt. Mater. **6**, 1701292 (2018).
16. Y. Li, C. T. Chan, and E. Mazur, "Dirac-like cone-based electromagnetic zero-index metamaterials," Light Sci. Appl. **10**, 203 (2021).
17. J. Luo and Y. Lai, "Hermitian and non-Hermitian Dirac-like cones in photonic and phononic structures," Front. Phys. **10**, 845624 (2022).
18. M. A. Vincenti, D. de Ceglia, A. Ciattoni, and M. Scalora, "Singularity-driven second- and third-harmonic generation at ε-near-zero crossing points," Phys. Rev. A **84**, 063826 (2011).
19. A. Ciattoni and E. Spinozzi, "Efficient second-harmonic generation in micrometer-thick slabs with indefinite permittivity," Phys. Rev. A **85**, 043806 (2012).
20. C. Argyropoulos, G. D. Aguanno, and A. Alù, "Giant second-harmonic generation efficiency and ideal phase matching with a double ε-near-zero cross-slit metamaterial," Phys. Rev. B **89**, 235401 (2014).
21. A. Capretti, Y. Wang, N. Engheta, and L. Dal Negro, "Comparative study of second-harmonic generation from epsilon-near-zero indium tin oxide and titanium nitride nanolayers excited in the near-infrared spectral range," ACS Photonics **2**, 1584–1591 (2015).
22. M. A. Vincenti, M. Kamandi, D. de Ceglia, C. Guclu, M. Scalora, and F. Capolino, "Second-harmonic generation in longitudinal epsilon-near-zero materials," Phys. Rev. B **96**, 045438 (2017).
23. H. Suchowski, K. O'Brien, Z. J. Wong, A. Salandrino, X. Yin, and X. Zhang, "Phase mismatch-free nonlinear propagation in optical zero-index materials," Science **342**, 1223–1226 (2013).
24. M. Z. Alam, I. De Leon, and R. W. Boyd, "Large optical nonlinearity of indium tin oxide in its epsilon-near-zero region," Science **352**, 795–797 (2016).
25. M. Z. Alam, S. A. Schulz, J. Upham, I. De Leon, and R. W. Boyd, "Large optical nonlinearity of nanoantennas coupled to an epsilon-near-zero material," Nat. Photonics **12**, 79–83 (2018).
26. Y. Yang, J. Lu, A. Manjavacas, T. S. Luk, H. Liu, K. Kelley, J. Maria, E. L. Runnerstrom, M. B. Sinclair, S. Ghimire, and I. Brener, "High-harmonic generation from an epsilon-near-zero material," Nat. Phys. **15**, 1022–1026 (2019).
27. X. Wen, G. Li, C. Gu, J. Zhao, S. Wang, C. Jiang, S. Palomba, C. M. De Sterke, and Q. Xiong, "Doubly enhanced second harmonic generation through structural and epsilon-near-zero resonances in TiN nanostructures," ACS Photonics **5**, 2087–2093 (2018).
28. C. K. Dass, H. Kwon, S. Vangala, E. M. Smith, J. W. Cleary, J. Guo, A. Alù, and J. R. Hendrickson, "Gap-plasmon-enhanced second-harmonic generation in epsilon-near-zero nanolayers," ACS Photonics **7**, 174–179 (2020).
29. J. Deng, Y. Tang, S. Chen, K. Li, A. V. Zayats, and G. Li, "Giant enhancement of second-order nonlinearity of epsilon-near-zero medium by a plasmonic metasurface," Nano Lett. **20**, 5421–5427 (2020).
30. D. Rocco, C. De Angelis, D. de Ceglia, L. Carletti, M. Scalora, and M. A. Vincenti, "Dielectric nanoantennas on epsilon-near-zero substrates: impact of losses on second order nonlinear processes," Opt. Commun. **456**, 124570 (2020).
31. J. Bohn, T. S. Luk, C. Tollerton, S. W. Hutchings, I. Brener, S. Horsley, W. L. Barnes, and E. Hendry, "All-optical switching of an epsilon-near-zero plasmon resonance in indium tin oxide," Nat. Commun. **12**, 1017 (2021).
32. W. Jia, M. Liu, Y. Lu, X. Feng, Q. Wang, X. Zhang, Y. Ni, F. Hu, M. Gong, X. Xu, Y. Huang, W. Zhang, Y. Yang, and J. Han, "Broadband terahertz wave generation from an epsilon-near-zero material," Light Sci. Appl. **10**, 11 (2021).
33. D. M. Solís, R. W. Boyd, and N. Engheta, "Dependence of the efficiency of the nonlinear-optical response of materials on their linear permittivity and permeability," Laser Photonics Rev. **15**, 2100032 (2021).
34. S. Suresh, O. Reshef, M. Z. Alam, J. Upham, M. Karimi, and R. W. Boyd, "Enhanced nonlinear optical responses of layered epsilon-near-zero metamaterials at visible frequencies," ACS Photonics **8**, 125–129 (2021).
35. J. B. Khurgin, M. Clerici, and N. Kinsey, "Fast and slow nonlinearities in epsilon-near-zero materials," Laser Photonics Rev. **15**, 2000291 (2021).
36. D. Genchi, I. G. Balasa, T. Cesca, and G. Mattei, "Tunable third-order nonlinear optical response in ε-near-zero multilayer metamaterials," Phys. Rev. Appl. **16**, 064020 (2021).
37. K. Wang, A. Liu, H. Hsiao, C. Genet, and T. Ebbesen, "Large optical nonlinearity of dielectric nanocavity-assisted Mie resonances strongly coupled to an epsilon-near-zero mode," Nano Lett. **22**, 702–709 (2022).
38. J. R. Gagnon, O. Reshef, D. H. G. Espinosa, M. Z. Alam, D. I. Vulis, E. N. Knall, J. Upham, Y. Li, K. Dolgaleva, E. Mazur, and R. W. Boyd, "Relaxed phase-matching constraints in zero-index waveguides," Phys. Rev. Lett. **128**, 203902 (2022).
39. J. I. Dadap, J. Shan, K. B. Eisenthal, and T. F. Heinz, "Second-harmonic Rayleigh scattering from a sphere of centrosymmetric material," Phys. Rev. Lett. **83**, 4045–4048 (1999).
40. G. Bachelier, J. Butet, I. Russier-Antoine, C. Jonin, E. Benichou, and P. F. Brevet, "Origin of optical second-harmonic generation in spherical gold nanoparticles: local surface and nonlocal bulk contributions," Phys. Rev. B **82**, 235403 (2010).
41. J. Song, J. Luo, and Y. Lai, "Side scattering shadow and energy concentration effects of epsilon-near-zero media," Opt. Lett. **43**, 1738–1741 (2018).

42. J. Luo, W. Lu, Z. Hang, H. Chen, B. Hou, Y. Lai, and C. T. Chan, "Arbitrary control of electromagnetic flux in inhomogeneous anisotropic media with near-zero index," Phys. Rev. Lett. **112**, 073903 (2014).
43. T. Dong, J. Luo, H. Chu, X. Xiong, R. Peng, M. Wang, and Y. Lai, "Breakdown of Maxwell Garnett theory due to evanescent fields at deep-subwavelength scale," Photonics Res. **9**, 848–855 (2021).
44. H. C. van de Hulst, *Light Scattering by Small Particles* (Dover, 1981).
45. D. J. Griffiths, *Introduction to Electrodynamics*, 3rd ed. (Prentice Hall, 1999).
46. A. V. Kildishev, A. Boltasseva, and V. M. Shalaev, "Planar photonics with metasurfaces," Science **339**, 1232009 (2013).
47. N. Yu and F. Capasso, "Flat optics with designer metasurfaces," Nat. Mater. **13**, 139–150 (2014).
48. S. Sun, Q. He, J. Hao, S. Xiao, and L. Zhou, "Electromagnetic metasurfaces: physics and applications," Adv. Opt. Photonics **11**, 380–479 (2019).
49. K. Du, H. Barkaoui, X. Zhang, L. Jin, Q. Song, and S. Xiao, "Optical metasurfaces towards multifunctionality and tunability," Nanophotonics **11**, 1761–1781 (2022).
50. P. Ahlberg, M. Hinnemo, M. Song, X. Gao, J. Olsson, S. L. Zhang, and Z. B. Zhang, "A two-in-one process for reliable graphene transistors processed with photo-lithography," Appl. Phys. Lett. **107**, 203104 (2015).
51. L. Z. Liu, S. B. Tian, Y. Z. Long, W. X. Li, H. F. Yang, J. J. Li, and C. Z. Gu, "Tunable periodic graphene antidot lattices fabricated by e-beam lithography and oxygen ion etching," Vacuum **105**, 21–25 (2014).
52. A. Harpale, M. Panesi, and H. B. Chew, "Plasma-graphene interaction and its effects on nanoscale patterning," Phys. Rev. B **93**, 035416 (2016).
53. M. F. El-Kady and R. B. Kaner, "Direct laser writing of graphene electronics," ACS Nano **8**, 8725–8729 (2014).
54. J. J. Dean and H. M. van Driel, "Second harmonic generation from graphene and graphitic films," Appl. Phys. Lett. **95**, 261910 (2009).
55. S. A. Mikhailov and K. Ziegler, "Nonlinear electromagnetic response of graphene: frequency multiplication and the self-consistent-field effects," J. Phys. Condens. Matter **20**, 384204 (2008).
56. A. Y. Bykov, T. V. Murzina, M. G. Rybin, and E. D. Obraztsova, "Second harmonic generation in multilayer graphene induced by direct electric current," Phys. Rev. B **85**, 121413 (2012).
57. Y. Q. An, J. E. Rowe, D. B. Dougherty, J. U. Lee, and A. C. Diebold, "Optical second-harmonic generation induced by electric current in graphene on Si and SiC substrates," Phys. Rev. B **89**, 115310 (2014).
58. J. J. Dean and H. M. van Driel, "Graphene and few-layer graphite probed by second-harmonic generation: theory and experiment," Phys. Rev. B **82**, 125411 (2010).
59. E. Sachet, C. T. Shelton, J. S. Harris, B. E. Gaddy, D. L. Irving, S. Curtarolo, B. F. Donovan, P. E. Hopkins, P. A. Sharma, A. L. Sharma, J. Ihlefeld, S. Franzen, and J. Maria, "Dysprosium-doped cadmium oxide as a gateway material for mid-infrared plasmonics," Nat. Mater. **14**, 414–420 (2015).
60. M. Wuttig, H. Bhaskaran, and T. Taubner, "Phase-change materials for non-volatile photonic applications," Nat. Photonics **11**, 465–476 (2017).
61. Z. Ma, H. Fan, H. Zhou, M. Huang, and J. Luo, "Broadband perfect transparency-to-absorption switching in tilted anisotropic metamaterials based on the anomalous Brewster effect," Opt. Express **29**, 39186–39199 (2021).
62. H. Fan, J. Li, Y. Lai, and J. Luo, "Optical Brewster metasurfaces exhibiting ultrabroadband reflectionless absorption and extreme angular asymmetry," Phys. Rev. Appl. **16**, 044064 (2021).
63. P. Nukala, M. Ren, R. Agarwal, J. Berger, G. Liu, A. T. C. Johnson, and R. Agarwal, "Inverting polar domains via electrical pulsing in metallic germanium telluride," Nat. Commun. **8**, 15033 (2017).
64. G. Grinblat, "Nonlinear dielectric nanoantennas and metasurfaces: frequency conversion and wavefront control," ACS Photonics **8**, 3406–3432 (2021).
65. Q. W. Lin, H. Wong, L. Huitema, and A. Crunteanu, "Coding metasurfaces with reconfiguration capabilities based on optical activation of phase-change materials for terahertz beam manipulations," Adv. Opt. Mater. **10**, 2101699 (2022).
66. M. Jafari and M. Rais-Zadeh, "Zero-static-power phase-change optical modulator," Opt. Lett. **41**, 1177–1180 (2016).
67. X. Sun, E. Thelander, J. W. Gerlach, U. Decker, and B. Rauschenbach, "Crystallization kinetics of GeTe phase-change thin films grown by pulsed laser deposition," J. Phys. D **48**, 295304 (2015).
68. R. Ma, D. S. Sutherland, and Y. Shi, "Harmonic generation in transition metal dichalcogenides and their heterostructures," Mater. Today **50**, 570–586 (2021).
69. R. Zhou, A. Krasnok, N. Hussain, S. Yang, and K. Ullah, "Controlling the harmonic generation in transition metal dichalcogenides and their heterostructures," Nanophotonics **11**, 3007–3034 (2022).
70. K. J. Palm, T. Gong, C. Shelden, E. Deniz, L. J. Krayer, M. S. Leite, and J. N. Munday, "Achieving scalable near-zero-index materials," Adv. Photonics Res. **3**, 2200109 (2022).
71. J. D. Caldwell, L. Lindsay, V. Giannini, I. Vurgaftman, T. L. Reinecke, S. A. Maier, and O. J. Glembocki, "Low-loss, infrared and terahertz nanophotonics using surface phonon polaritons," Nanophotonics **4**, 44–68 (2015).
72. H. Husu, R. Siikanen, J. Mäkitalo, J. Lehtolahti, J. Laukkanen, M. Kuittinen, and M. Kauranen, "Metamaterials with tailored nonlinear optical response," Nano Lett. **12**, 673–677 (2012).
73. K. Konishi, T. Higuchi, J. Li, J. Larsson, S. Ishii, and M. Kuwata-Gonokami, "Polarization-controlled circular second-harmonic generation from metal hole arrays with threefold rotational symmetry," Phys. Rev. Lett. **112**, 135502 (2014).
74. K. Yao, N. R. Finney, J. Zhang, S. L. Moore, L. Xian, N. Tancogne-Dejean, F. Liu, J. Ardelean, X. Xu, D. Halbertal, K. Watanabe, T. Taniguchi, H. Ochoa, A. Asenjo-Garcia, X. Zhu, D. N. Basov, A. Rubio, C. R. Dean, J. Hone, and P. J. Schuck, "Enhanced tunable second harmonic generation from twistable interfaces and vertical superlattices in boron nitride homostructures," Sci. Adv. **7**, eabe8691 (2021).
75. S. Lan, S. Rodrigues, Y. Cui, L. Kang, and W. Cai, "Electrically tunable harmonic generation of light from plasmonic structures in electrolytes," Nano Lett. **16**, 5074–5079 (2016).
76. J. W. You and N. C. Panoiu, "Tunable and dual-broadband giant enhancement of second-harmonic and third-harmonic generation in an optimized graphene-insulator-graphene metasurface," Phys. Rev. B **102**, 121403 (2020).
77. A. S. Kadochkin, A. S. Shalin, and P. Ginzburg, "Granular permittivity representation in extremely near-field light-matter interaction processes," ACS Photonics **4**, 2137–2143 (2017).
78. Y. Li, Y. Rao, K. F. Mak, Y. You, S. Wang, C. R. Dean, and T. F. Heinz, "Probing symmetry properties of few-layer MoS_2 and h-BN by optical second-harmonic generation," Nano Lett. **13**, 3329–3333 (2013).
79. A. R. Khan, B. Liu, L. Zhang, Y. Zhu, X. He, L. Zhang, T. Lü, and Y. Lu, "Extraordinary temperature dependent second harmonic generation in atomically thin layers of transition-metal dichalcogenides," Adv. Opt. Mater. **8**, 2000441 (2020).
80. W. Wu, L. Wang, Y. Li, F. Zhang, L. Lin, S. Niu, D. Chenet, X. Zhang, Y. Hao, T. F. Heinz, J. Hone, and Z. L. Wang, "Piezoelectricity of single-atomic-layer MoS_2 for energy conversion and piezotronics," Nature **514**, 470–474 (2014).
81. I. Paradisanos, A. M. S. Raven, T. Amand, C. Robert, P. Renucci, K. Watanabe, T. Taniguchi, I. C. Gerber, X. Marie, and B. Urbaszek, "Second harmonic generation control in twisted bilayers of transition metal dichalcogenides," Phys. Rev. B **105**, 115420 (2022).